JOURNAL OF ENVIRONMENTAL SCIENCES 33 (2015) 169–178

Available online at www.sciencedirect.com

ScienceDirect

www.journals.elsevier.com/journal-of-environmental-sciences

JOURNAL OF ENVIRONMENTAL SCIENCES

www.jesc.ac.cn

Photocatalytic decomposition of acrylonitrile with N–F codoped TiO_2/SiO_2 under simulant solar light irradiation

*Dandan Pang, Lu Qiu, Yunteng Wang, Rongshu Zhu, Feng Ouyang**

Shenzhen Graduate School, Harbin Institute of Technology, Shenzhen 518055, China

ARTICLE INFO

Article history:
Received 6 October 2014
Revised 20 December 2014
Accepted 14 January 2015
Available online 6 May 2015

Keywords:
Photocatalytic activity
Acrylonitrile
In situ IR
N–F codoping

ABSTRACT

The solid acid catalyst, N–F codoped TiO_2/SiO_2 composite oxide was prepared by a sol–gel method using NH_4F as nitrogen and fluorine source. The prepared materials were characterized by X-ray diffraction (XRD), scanning electron microscopy (SEM), X-ray photoelectron spectroscopy (XPS), UV–Visible diffuse reflectance spectroscopy (UV–Vis), ammonia adsorption and temperature-programmed desorption (NH_3-TPD), *in situ* Fourier transform infrared spectroscopy (FT-IR) and N_2 physical adsorption isotherm. The photocatalytic activity of the catalyst for acrylonitrile degradation was investigated under simulant solar irradiation. The results showed that strong Lewis and Brønsted acid sites appear on the surface of the sample after N–F doping. Systematic investigation showed that the highest photocatalytic activity for acrylonitrile degradation was obtained for samples calcined at 450°C with molar ratio (NH_4F to Ti) of 0.8. The degradation ratio of 71.5% was achieved with the prepared catalyst after 6-min irradiation, demonstrating the effectiveness of photocatalytic degradation of acrylonitrile with N–F codoped TiO_2/SiO_2 composite oxide. The photocatalyst is promising for application under solar light irradiation. Moreover, the intermediates generated after irradiation were verified by gas chromatography–mass spectrometry (GC–MS) analysis and UV–Vis spectroscopy to be simple organic acids with lower toxicity, and the degradation pathway was also proposed for acrylonitrile degradation with the prepared catalyst.

Introduction

Acrylonitrile (CH_2═CH–CN) is considered as a hazardous pollutant since it is mutagenic, carcinogenic and teratogenic to human beings (Léonard et al., 1999). The health authorities of the Federal Republic of Germany have placed acrylonitrile in the category of carcinogenic chemicals for which no threshold limits are established. The US EPA has classified acrylonitrile as a "priority water pollutant" and "hazardous air pollutant".

Traditional control technologies for acrylonitrile include adsorption and desorption (Huang et al., 1999), thermal and catalytic incineration at high temperatures (Gervasini and Ragaini, 2000; Hung and Chu, 2006) and biotechnological abatement methods (Zhang and Pierce, 2009). There are many limitations including high operating costs, secondary waste stream problems, *etc.* Therefore, developing an alternative abatement method such as photocatalytic oxidation attracts increasing interest.

To date, TiO_2 has been the most widely used photocatalyst due to its ability to convert UV light to chemical energy to decompose most organic pollutants that exist in air and aqueous systems or to generate hydrogen from water (Macwan et al., 2011). The general drawbacks of photocatalytic

* *Corresponding author*. E-mail: ouyangfh@hit.edu.cn (Feng Ouyang).

http://dx.doi.org/10.1016/j.jes.2015.01.017

oxidation, such as low reaction rates, require improvement. The photocatalytic activity of TiO_2 can be improved by the addition of SiO_2, which increases the available surface area of the catalyst (Chen et al., 2004). Another potentially effective way to improve the photocatalyst performance is to increase the number of surface acid sites, because the photocatalytic activity has been shown to increase with catalyst surface acidity. Doping TiO_2 with metal oxides was reported to increase the surface acidity and photocatalytic activity of TiO_2 (Cui et al., 1995). Sulfated TiO_2 can be readily synthesized by the reaction of amorphous TiO_2 with sulfur compounds at high temperatures and employed as a photocatalyst (Wang et al., 2006a). However, little work has been done to study the photocatalytic degradation of acrylonitrile on acid catalysts. F-doped silica-supported TiO_2 was used for photocatalytic decomposition of acrylonitrile under simulant solar light irradiation (Pang et al., 2014). Gas-phase photocatalytic oxidation of acrylonitrile on sulfated TiO_2 was also reported (Jõks et al., 2011).

In this study, solid acid catalyst, N–F codoped TiO_2/SiO_2 composite oxide was synthesized by sol–gel method. The objective of the present research was to determine the effectiveness of photocatalytic degradation of acrylonitrile with N–F codoped TiO_2/SiO_2 composite oxides. The declared objective was achieved by experimental research on effects of two variables – calcination temperature and NH_4F ratio in the starting material – on the photocatalytic activity of the prepared catalysts for acrylonitrile degradation. The identification of the intermediates of photocatalytic oxidation of acrylonitrile was carried out and mechanisms for the degradation process were also proposed.

1. Experimental

1.1. Preparation of photocatalysts

Silica gel (100–200 mesh, Qingdao Haiyang Chemical Co., Ltd., China) was obtained for TiO_2 loading. All other chemicals were of analytical reagent grade quality and were employed without further purification. All aqueous solutions were prepared in deionized water from a Milli-Q water system.

The TiO_2/SiO_2 composite powders were prepared by sol–gel method. Solution A was obtained by mixing 10 mL anhydrous alcohol, 0.5 mL deionized water and 2 mL acetic acid. Solution B was obtained by dissolving the starting material of 5 mL tetrabutyl titanate ($Ti(OC_4H_9)_4$) in 13 mL anhydrous alcohol. Solution A was added dropwise in solution B with vigorous stirring for 2 hr to obtain the homogeneous transparent sol. 2.0 g silica gel was added to the sol with severe stirring for 1 hr (Chen et al., 2004). The resulting gelatinous solution was aged for 12 hr at room temperature and then dried at 80°C. The dry gel was then crushed and calcined at different temperatures for 2 hr. TiO_2/SiO_2 composite powders were thus obtained.

Ammonium fluoride (NH_4F) was used as the doping precursor as the nitrogen–fluorine source (Li et al., 2011) and the molar ratios of NH_4F to Ti (R_{NF}) were 0:1, 0.2:1, 0.4:1, 0.8:1 and 1.6:1. NH_4F aqueous solution (13.83 mol/L) was added in solution A and the same operation as above was conducted, and N–F codoped TiO_2/SiO_2 powders were thus obtained.

1.2. Characterization of photocatalysts

The X-ray diffraction patterns of the powders were obtained on an X-ray diffraction analyzer (D/max 2500, Rigaku Corporation, Japan) with Cu Kα X-ray source at a scanning rate of 8°/min in the 2θ range between 10° and 80°. The accelerating voltage and the applied current were 40 kV and 200 mA, respectively. Crystallite size was calculated according to the Scherrer equation (Gu et al., 2004; Tai et al., 2004):

$$L = \frac{K\lambda}{B\cos\theta} \quad (1)$$

where, $B^2 = B^2_{measured} - b^2_{instrumental}$, L, K, λ and θ are the average crystal size, a shape factor of 0.9 for spherical crystallites, the X-ray wavelength (0.15405 nm) and Bragg diffraction angle, respectively. B, $B_{measured}$ and $b_{instrumental}$ are the breadths of the intrinsic diffraction profile, test sample diffraction integral profile and instrumental diffraction profile, respectively. The value of b for the D/max 2500 Diffractometer is 0.0033 arcs. The morphology was examined using a scanning electron microscope (S4700, Hitachi, Japan). The XPS (PHI-1800, ULVAC-PHI, Japan) measurements were performed with monochromatic Al $K\alpha$ excitation, and all the bonding energies were calibrated to the C 1s peak at 284.6 eV. UV–Visible diffuse reflectance spectra of the powders were collected with a UV–Vis Spectrophotometer (UV–2540, Shimadzu Corporation, Japan) over the spectral range of 240–800 nm. $BaSO_4$ was used as a reference. The BET specific surface area was measured by nitrogen gas adsorption at 77 K using an adsorption instrument (BELSOROP-MINI II, Ankersmid, Holland). Pore volume and pore size distribution were determined by the Barrett–Joyner–Halenda (BJH) method.

The nature of acid sites was investigated using pyridine as the probe molecule. Fourier transform infrared spectra were recorded using an infrared spectrometer (Nicolet 380, Thermo Fisher Scientific, USA) with a resolution of 4 cm^{-1} and 32 scans in the region of 4000–1000 cm^{-1}. Self-supported wafers of the samples were prepared by applying 11 ton pressure. The sample was subjected to vacuum (10^{-2} mbar) in the sample holder followed by thermal treatment at 400°C for 2 hr to obtain a clean surface. The adsorption of pyridine was done at 180°C for 40 min. The physisorbed pyridine was then desorbed under vacuum at room temperature.

The NH_3-TPD technique was used for the quantitation of the total surface acidity. The sample was preheated at 400°C for 2 hr to remove organic compounds. Ammonia was adsorbed at 100°C and excess ammonia was purged by helium. The measurement of acid site density was carried out by heating from 100 to 600°C at 15°C/min. The desorbed ammonia was reacted with a 0.05 mol/L HCl solution that was then back-titrated with 0.05 mol/L NaOH solution (Al-Yassir et al., 2005; Le Van Mao et al., 2006).

In order to investigate the recombination and lifespan of photogenerated electrons-holes in the semiconductor, the photoluminescence (PL) emission spectra of the samples were measured at room temperature by a Raman spectrometer (inVia, Renishaw, England) illuminated with a 325 nm He–Cd laser.

Identification of products was verified using gas chromatography–mass spectrometry (GC–MS) (Thermo trace GC-DSQ Tune, Thermo Fisher Scientific, USA). The solution after irradiation was extracted using chloroform. Then the extract was filtered through a 0.45 μm filter and stored at 4°C until instrumental analysis was conducted. The (GC–MS) was equipped with a DB-WAX capillary column (30 m, 0.25 mm internal diameter, 0.25 μm film thickness) and electron ionization (EI) detector. The temperature of the injector and the MS-transfer were both held at 200°C. Mass spectra were compared with those in the GC–MS database for compound identification.

1.3. Photocatalytic experiments

Photocatalytic reaction was carried out in a self-made cylindrical glass reactor using a 350 W xenon arc lamp (AHD350, Shenzhen AnHongDa Opto Technology Co., Ltd., China) as simulant solar light. A typical degradation experiment was carried out as follows: the catalyst was added to 180 mL of aqueous solution of acrylonitrile with an initial concentration of 10 mg/L. The reactor was sealed. The reaction mixture was stirred for 60 min in the dark to reach adsorption equilibrium. Then the cooling water system and the xenon lamp were turned on. A small amount of solution was periodically withdrawn from the reaction mixture with a syringe and filtered through a 0.45 μm filter for high performance liquid chromatography (HPLC) analysis.

1.4. Analytical methods

The acrylonitrile concentration in the solution was quantified using an HPLC (LC2000, Shanghai TianMei Scientific Instruments Co., Ltd., China) equipped with a LC-2030 UV detector and a Sunfire™ C18 column (150 mm, 4.6 mm id.). The eluent was composed of methanol (30%) and water (70%). The flow rate was kept at 1.0 mL min^{-1}. The absorption spectra showed absorption maxima at 197 nm for acrylonitrile, but the detection wavelength selected for acrylonitrile was 210 nm to remove the noise from methanol with the cutoff wavelength of 205 nm.

In general, at low substrate concentration, the kinetics of the photocatalytic oxidation process is described well by a pseudo-first-order equation (Chen et al., 2004).

$$\ln\left(\frac{C_o}{C_t}\right) = k_{app}t \quad (2)$$

where C_o, C_t, t and k_{app} are the reactant concentration after the system reaches adsorption equilibrium (mg/L), the reactant concentration at time t (mg/L), the irradiation time (min) and the apparent pseudo-first-order rate constant (min^{-1}), respectively.

The degradation ratio of the reactant was also used to evaluate the photocatalytic activity of a sample:

$$D = \frac{C_o - C_t}{C_o} \times 100\% \quad (3)$$

where D is the degradation ratio of the reactant.

2. Results and discussion

2.1. SEM images

Fig. 1 presents the SEM images of pure TiO_2, TiO_2/SiO_2, and N–F codoped TiO_2/SiO_2 calcined at 450°C. Pure TiO_2 was irregularly agglomerated from primary particles. The TiO_2/SiO_2 possessed a rough and porous surface, resulting in higher surface area than pure TiO_2. Additionally, pure TiO_2 and TiO_2/SiO_2 showed the formation of secondary particles by the agglomeration of primary particles. However, N–F codoped TiO_2/SiO_2, consisting of solid microspheres, showed little agglomeration and did not collapse. The agglomerate size of N–F codoped TiO_2/SiO_2 was smaller than that of TiO_2/SiO_2. Guo et al. reported that ammonium fluoride could modify the zeta potential of spherical poly-condensed titania species generated at the initial stage of the hydrolysis reaction (Guo et al., 2003). The results show that NH_4F as N–F doping precursor can inhibit the agglomeration of TiO_2 powder effectively, which is beneficial for higher activity.

2.2. XPS analysis

Fig. 2 shows XPS spectra of N–F codoped TiO_2/SiO_2 with R_{NF} of 0.8 calcined at 450°C. The binding energies of Ti 2p3/2 and Ti 2p1/2 are equal to 458.7 and 464.5 eV, respectively (Fig. 2a), indicating that Ti exists in the Ti^{4+} form (Wu et al., 2010; Xiang et al., 2010; Xie et al., 2007). The O 1s signal is shown in Fig. 2b. The peak at 529.9 eV corresponds to lattice oxygen of TiO_2, and a strong peak centered at 533.2 eV is assigned to surface hydroxides (Xie et al., 2007). Fig. 2c presents the F 1s XPS spectra. The F 1s region is composed of two contributions. One peak located around 687.7 eV is attributed to the substitute F atoms that occupied oxygen sites in the TiO_2 crystal lattice (Huang et al., 2006; Wu et al., 2010; Xie et al., 2007). This indicates that F atoms are incorporated into the crystal lattice of TiO_2 prepared by the sol–gel method using NH_4F as precursor. Another peak located at 684.2 eV is originated from F^- ions physically adsorbed on the surface of TiO_2 (≡Ti–F) (Wu et al., 2010; Xiang et al., 2010). The surface ≡Ti–F group may act as an electron-trapping site and reduce interfacial electron transfer rates *via* tightly holding trapped electrons due to the strong electronegativity of the fluorine (Park and Choi, 2004; Xiang et al., 2010). Fig. 2d shows the XPS spectra for the N 1s. The peak appearing at 400.0 eV is greater than the typical binding energy of 396.9 eV in TiN (Saha and Tomkins, 1992). It should be assigned to the formation of a N–Ti–O linkage (Jang et al., 2006; Wang et al., 2006b; Xie et al., 2007). When nitrogen replaces oxygen in the O–Ti–O structure, the electron density around N is reduced. Thus, the N 1s binding energy in an O–Ti–N environment is higher than that in a N–Ti–N environment (Wang et al., 2006b). The actual amounts of F and N in the sample are 1.9% and 0.5%, respectively.

2.3. Nitrogen physical adsorption

Fig. 3 presents Nitrogen adsorption and desorption isotherms of N–F codoped TiO_2 without SiO_2 and N–F codoped TiO_2/SiO_2 nanoparticles calcined at 450°C. According to

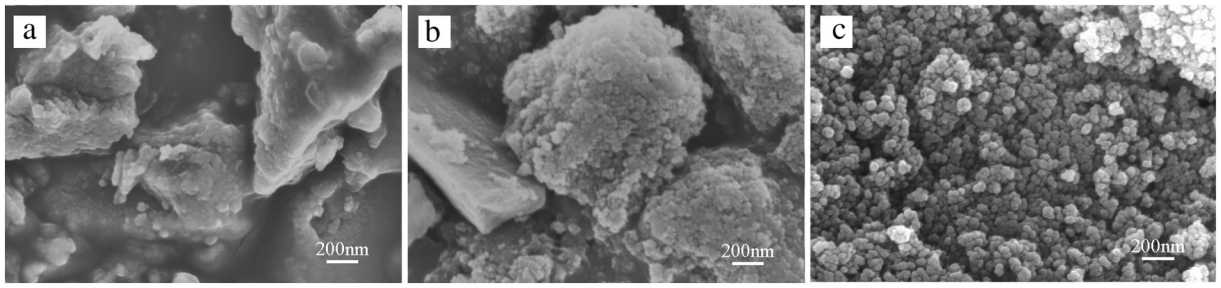

Fig. 1 – SEM images of (a) pure TiO_2, (b) TiO_2/SiO_2 and (c) N–F codoped TiO_2/SiO_2 with molar ratio (NH_4F to Ti) of 0.8.

IUPAC classification, N–F codoped TiO_2 and N–F codoped TiO_2/SiO_2 nanoparticles display type IV isotherms and H2 hysteresis, which indicate the presence of mesoporous materials (Gregg and Sing, 1997). The plot of the pore size distribution (inset in Fig. 3) was determined by using the Barrett–Joyner–Halenda (BJH) method from the adsorption branch of the isotherm. It shows that both clearly have a mesoporous structure. The mesoporous structure is probably formed by agglomeration of primary particles (interparticle pores) (Wu et al., 2010). The average pore diameters of N–F codoped TiO_2/SiO_2 and N–F codoped TiO_2 nanoparticles are both 8.0 nm. However, the specific surface area of the former (214 m^2/g) is significantly higher than that of the latter (60 m^2/g).

2.4. UV–Vis analysis

Fig. 4 shows the UV–Vis diffuse reflection spectra of TiO_2/SiO_2 and N–F codoped TiO_2/SiO_2 calcined at 450°C, respectively. The undoped TiO_2/SiO_2 obtained was a white powder. However, a slightly yellow color appeared for the N–F codoped catalyst. Generally, the color of a solid is determined by the

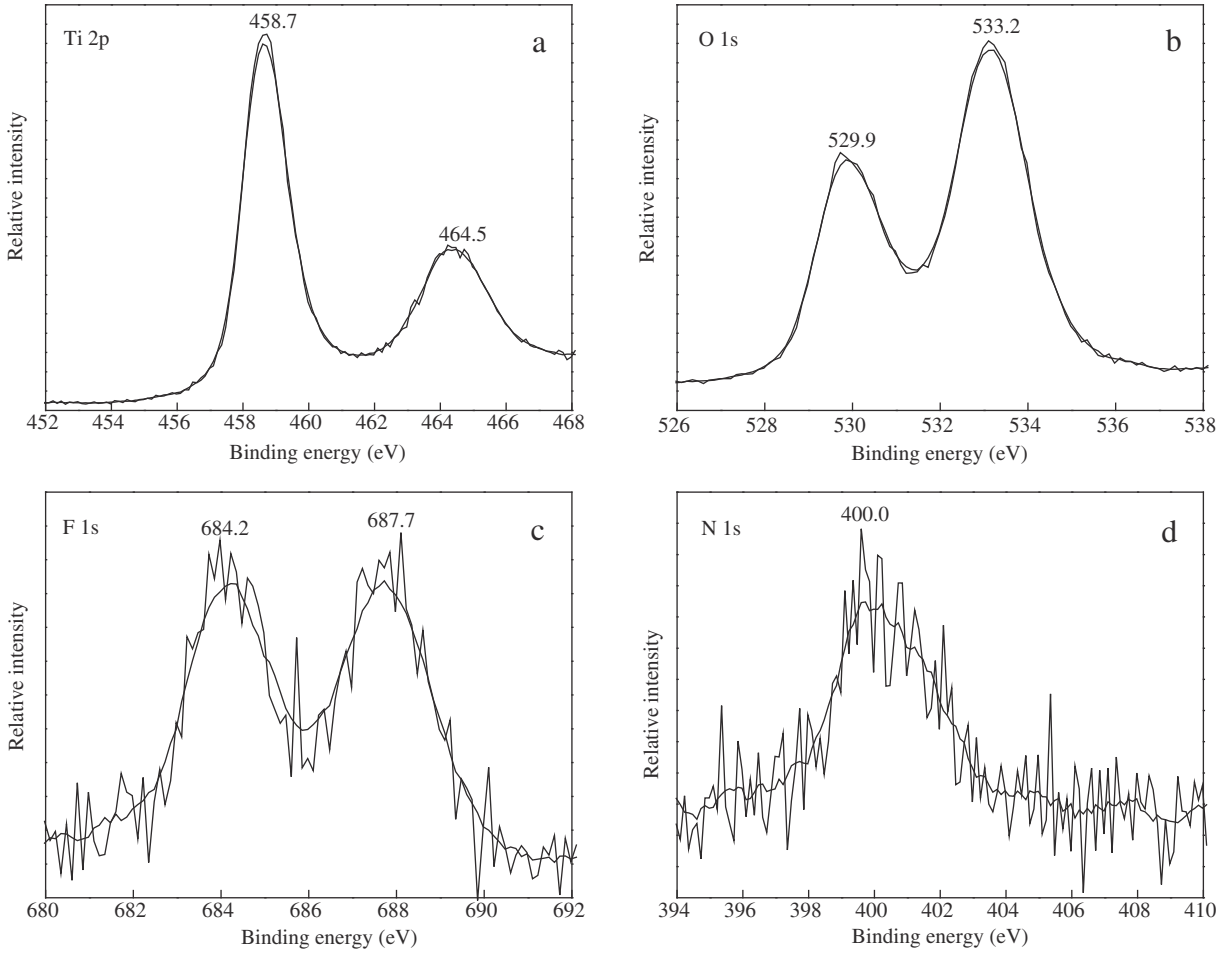

Fig. 2 – Ti 2p (a), O 1 (b), F 1s (c) and N 1s (d) high-resolution XPS spectra of N–F codoped TiO_2/SiO_2.

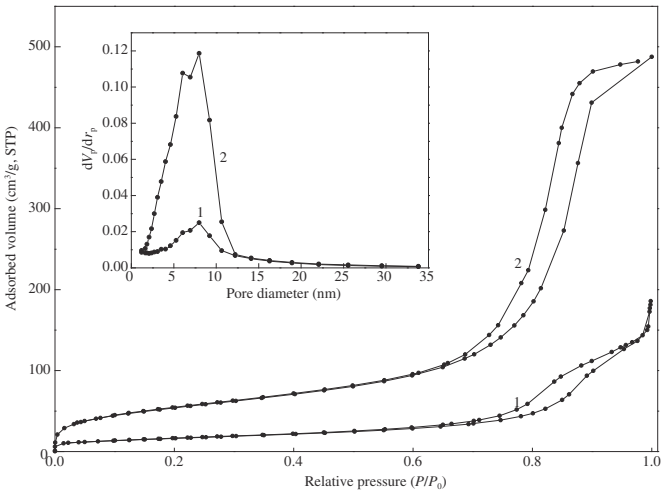

Fig. 3 – Nitrogen adsorption and desorption isotherms of (1) N–F codoped TiO_2 without SiO_2 and (2) N–F codoped TiO_2/SiO_2 nanoparticles. Inset shows Barrett–Joyner–Halenda (BJH) pore size distributions of the corresponding samples.

position of its absorption edge. The band gaps of the samples are determined by the following equation (O'Regan and Grätzel, 1991):

$$E_g = 1239.8/\lambda \quad (4)$$

where E_g and λ are the band gap and wavelength of the absorption edge in the spectrum, respectively. The absorption edge of the sample was shifted to longer wavelength after N–F doping. The absorption edge of the undoped TiO_2/SiO_2 occurred at around 388 nm. After N–F doping, the absorption edge of the sample occurred at around 414 nm and the band gap was changed to about 2.99 eV. The band gap narrowing of the doped sample should be attributed to doping N from ammonium fluoride, since F doping did not result in any significant shift in the fundamental absorption of TiO_2 (Huang et al., 2007; Li et al., 2005).

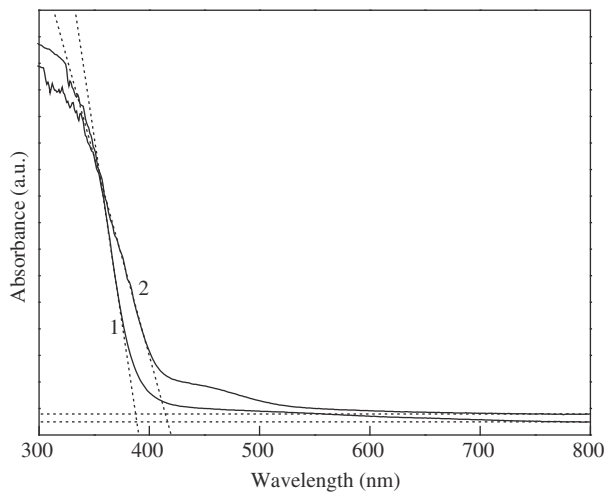

Fig. 4 – UV–Vis absorption spectra of (1) TiO_2/SiO_2 and (2) N–F codoped TiO_2/SiO_2.

2.5. *Effect of NH_4F ratio in starting material on physical and photocatalytic properties*

In situ characterization of surface species and surface active sites during heterogeneous photocatalytic processes is one of the most important experimental approaches. Many spectroscopic techniques have been employed to study photocatalytic reactions on the surface. Among these, FT-IR is probably the best method for *in situ* photocatalytic studies because it is inexpensive, sensitive, and capable of determining chemical species, and can be carried out at atmospheric pressure and room temperature. The adsorption of pyridine combined with

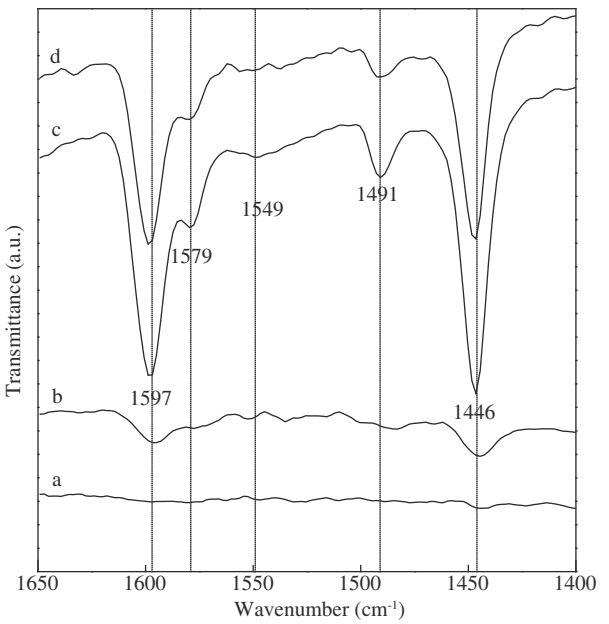

Fig. 5 – Infrared spectra of chemisorbed pyridine molecules adsorbed on the N–F codoped TiO_2/SiO_2 with NH_4F/Ti molar ratio of (a) 0:1, (b) 0.2:1, (c) 0.8:1 and (d) 1.6:1.

in situ FT-IR technique is well known for characterizing the surface Brønsted and Lewis acidic sites (Al-Yassir et al., 2005; Jin et al., 2009; Wang et al., 2006a). Fig. 5 shows the IR spectra of pyridine chemisorbed on the N–F codoped TiO_2/SiO_2 with different NH_4F/Ti molar ratios. The IR spectrum of Fig. 5c clearly displays the characteristic bands of the chemisorbed pyridine. The band observed at 1597 cm^{-1} is assigned to hydrogen-bonded pyridine (Al-Yassir et al., 2005). The bands at 1445 and 1579 cm^{-1} are due to the interaction of pyridine with strong and weak Lewis acid sites, respectively (Al-Yassir et al., 2005; Le Van Mao et al., 1999; Wang et al., 2006a). The peak at 1549 cm^{-1} is due to the vibration of pyridine adsorbed on Brønsted acid sites (Le Van Mao et al., 1999). The peak at 1491 cm^{-1} was assigned to pyridine adsorbed on both Lewis and Brønsted acid sites (Jin et al., 2009). Most notably, only one small peak at 1446 cm^{-1} corresponding to pyridine adsorbed on Lewis acid site was observed for the undoped sample (Fig. 5a). With the increase of NH_4F/Ti molar ratio, a significant increase in the intensity of the characteristic bands of pyridine was observed. This suggests that the surface acid sites can become stronger and react with more pyridine molecules after N–F doping. These strong Lewis and Brønsted acid sites provided better adsorption centers for oxygen and reactant molecules and converted adsorbed water into active hydroxyl groups, which improved the photocatalytic activity (Pelaez et al., 2012; Wang et al., 2006a). The Lewis acid sites are strong adsorption centers and can accept electron pairs. Acrylonitrile, with lone-pair electrons, can be easily adsorbed onto the Lewis acid sites and oxidized by ·OH. The Brønsted acid sites can donate protons (H^+) and generate ·OOH, a powerful oxidant. The ·OH and ·OOH formations are then involved in acrylonitrile oxidation reactions, leading to the decrease in the re-combination ratio of electrons and holes, as shown in Fig. 7. On the other hand, from the viewpoint of microscopic reaction kinetics, the stronger the adsorption ability of Lewis acid sites is, the longer the residence time of reactant molecules adsorbed on the surface and the higher the reaction activity.

Fig. 6 shows the distribution curves of the acid strength of the N–F codoped TiO_2/SiO_2 with different NH_4F/Ti molar ratios. The surface acid site densities of N–F codoped TiO_2/SiO_2 and undoped sample were calculated, as shown in Table 1. With the increase of NH_4F/Ti molar ratio, an increase for the amount of acid sites was observed. However, excess N–F doping results in the decrease in surface acid sites (Fig. 5d and Table 1). Essentially, the acidity profile of the N–F codoped samples exhibits three or four separated peaks, while that of the undoped sample shows only two desorption peaks. The last two peaks at about 450 and 510°C for N–F codoped samples (0.8:1 and 1.6:1) corresponding to stronger acid sites, possibly play a more important role in improving the photocatalytic activity.

Table 1 – Acid sites density of N–F codoped TiO_2/SiO_2 with NH_4F/Ti molar ratio of (a) 0:1, (b) 0.2:1, (c) 0.8:1 and (d) 1.6:1 calculated by using NH_3-TPD.

Samples	Peak temperature (°C)				Amount of desorbed NH_3 (mmol/g)				
	I	II	IV	V	I	II	IV	V	Total
(a)	155	327			0.11	0.04			0.15
(b)	199	268		498	0.07	0.08		0.12	0.27
(c)	205	302	438	505	0.25	0.09	0.13	0.24	0.71
(d)	208	290	468	520	0.13	0.14	0.08	0.16	0.51

I, II, IV, and V denote as the number of the peak.

PL emission spectra are widely used to determine the efficiency of charge carrier trapping, migration, transfer and separation, and the recombination of photogenerated electrons and holes in semiconductors (Xiang et al., 2010; Zhang et al., 2000). Fig. 7 shows a comparison of the PL spectra of undoped and N–F codoped TiO_2/SiO_2 samples prepared with varying R_{NF} values in the wavelength range of 450–650 nm. It is found that the PL emission intensity decreases with the increase of R_{NF}. However, the sample with excessive N–F doping exhibits an increase in emission intensity. This suggests that an appropriate amount of N–F doping will slow the radiative recombination rate of photogenerated electrons

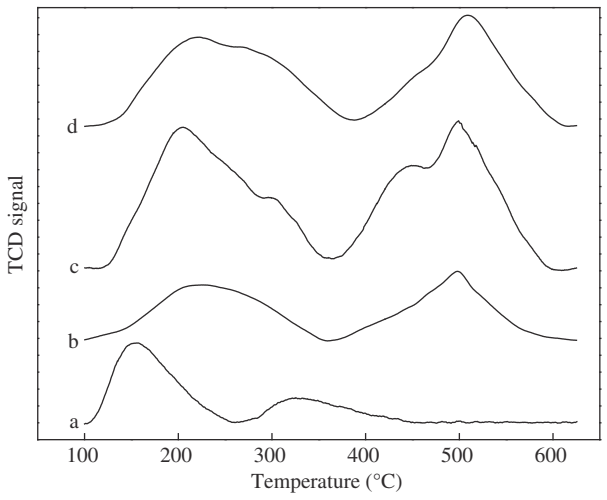

Fig. 6 – NH_3-TPD profile of N–F codoped TiO_2/SiO_2 with NH_4F/Ti molar ratio of (a) 0:1, (b) 0.2:1, (c) 0.8:1 and (d) 1.6:1.

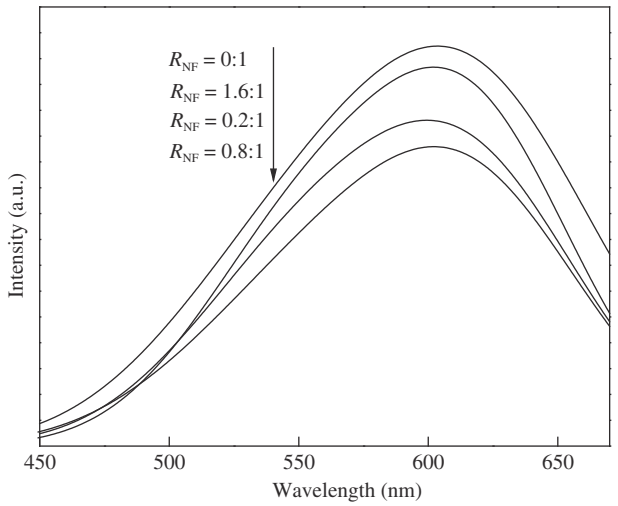

Fig. 7 – Photoluminescence emission spectra of N–F codoped TiO_2/SiO_2 composition oxides with different NH_4F/Ti molar ratio (R_{NF}).

and holes in the samples. Moreover, the lower the intensity of PL spectra, the higher the photocatalytic activity, which is consistent with earlier published reports (Xiang et al., 2010; Yu et al., 2002).

Fig. 8 shows the dependence of the photocatalytic activity of acrylonitrile degradation for 6 min irradiation over N–F codoped TiO_2/SiO_2 on the NH_4F/Ti molar ratio of the starting materials. The apparent rate constant increases with the NH_4F/Ti molar ratio to reach a maximum at NH_4F/Ti = 0.8, which is due to the increase of the surface acid sites on the sample after N–F doping (Fig. 5). However, excessive N–F doping results in the decrease in the photocatalytic activity, which is attributed to the introduction of new recombination centers (defect sites) of photogenerated electrons and holes (Fig. 7). There is an optimal dopant concentration, which is similar to the previous studies (Li et al., 2011; Maeda et al., 2005).

2.6. Effect of calcination temperature on photocatalytic activity

Fig. 9 shows the XRD patterns of N–F codoped TiO_2/SiO_2 powders prepared at different calcination temperatures. All N–F codoped TiO_2/SiO_2 powders contained only anatase phase TiO_2, and no phase transformation from anatase to rutile was observed, even after calcination at 650°C for 2 hr. Moreover, the peak intensity of anatase increased with the increase of calcination temperature and the peaks became sharper, suggesting that the relative crystallinity and crystalline size significantly increased. The average crystallite sizes of samples can be calculated by the Scherrer equation using the full-width at half-maximum of the X-ray diffraction peaks at $2\theta = 25.2°$. The average crystallite size increased with the increase of calcination temperature. However, the surface area decreased as the calcination temperature increased (Table 2).

Fig. 10 shows the effect of calcination temperature on the photocatalytic activity of N–F co-doped TiO_2/SiO_2 for 6 min irradiation. It can be observed that the photocatalytic activity of N–F codoped TiO_2/SiO_2 for acrylonitrile photodegradation increased with the increase of calcination temperature, and reached a maximum at the calcination temperature of 450°C.

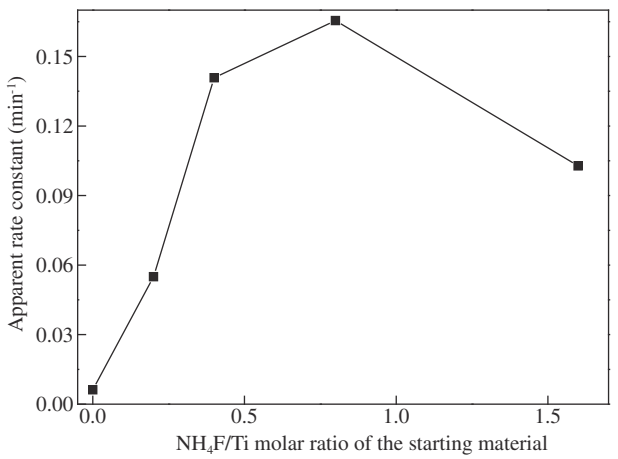

Fig. 8 – Dependence of the photocatalytic activity of acrylonitrile degradation over N–F codoped TiO_2/SiO_2 calcined at 450°C on the NH_4F/Ti molar ratio of starting materials.

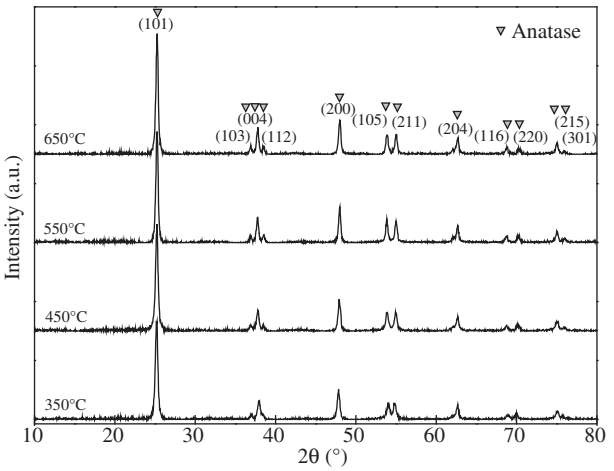

Fig. 9 – XRD patterns of N–F codoped TiO_2/SiO_2 samples calcined at 350, 450, 550 and 650°C.

It appears that the increase in photocatalytic activity at higher calcination temperature is mainly due to the higher crystallinity of the powder (Fig. 9), which results in a decrease in the defect density on the catalyst surface (Maeda et al., 2005). Meanwhile, with further increasing calcination temperature, the average crystal size of the N–F codoped TiO_2/SiO_2 catalyst increased. However, the photocatalytic activity decreased. This implies that besides the higher crystallinity, suitable defect density is also essential for high photocatalytic activity. This is consistent with the nature of the surface acid sites (Fig. 5). We consider that surface acid sites are related to surface defects. The surface defects are generated by the coordination of different surface atoms. The difference in surface charge distribution may cause the formation of different types of surface acid sites (Brønsted and Lewis acid sites).

2.7. Influence on the photocatalytic activities of light absorption properties of N–F codoped TiO_2/SiO_2

Fig. 11 shows the degradation of acrylonitrile in the presence of undoped and N–F codoped samples under simulant solar light and UV irradiation ($\lambda \leq 400$ nm), respectively. The N–F codoped TiO_2/SiO_2 photocatalyst exhibits higher activity than the undoped sample, and 71.5% and 64.3% acrylonitrile could be removed after 6 min under simulant solar light and UV irradiation, respectively. The above details suggest that the photocatalytic performance of TiO_2/SiO_2 composite oxide is greatly improved by N–F doping under simulant solar light and UV light irradiation, which demonstrates that high

Table 2 – Specific surface area and crystal size of N–F codoped TiO_2/SiO_2 powders at different calcination temperatures.

Calcination temperature (°C)	Specific surface area (m^2/g)	Crystal size (nm)
350	219	24.8
450	214	26.6
550	206	28.2
650	196	29.1

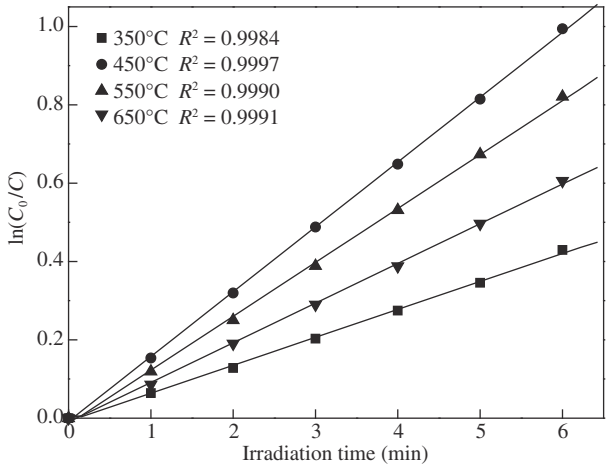

Fig. 10 – Effect of calcination temperature on photocatalytic activity of N–F codoped TiO_2/SiO_2.

activity is not only dependent on surface active sites but also related to the light absorption properties (Fig. 4). Though the shift of absorption edge is small, corresponding energy levels are suitable for an electron transition to generate ·OH; moreover, the interval of shift falls on the UV light region of the simulant solar light. This implies that the prepared catalyst may have the highest efficiency under irradiation of simulant solar light in the region. The catalyst may absorb enough strong light and excite electron transition, then cause a series of photochemical reactions, leading to degradation of a large amount of acrylonitrile.

2.8. Photocatalytic decomposition pathway of acrylonitrile

Many organic pollutants can be decomposed by photocatalytic oxidation process with low cost. However, the intermediates may be more toxic and unacceptable for human heath than their precursors. Therefore, it is necessary to identify the intermediates formed during the photocatalytic process. Krichevskaya et al. reported that the main products of gas-phase acrylonitrile photocatalytic oxidation included nitrogen dioxide, nitrous oxide, carbon dioxide, water, hydrogen cyanide and carbon monoxide by using Degussa P25 under UV irradiation (Krichevskaya et al., 2009). Jõks et al. reported that the gaseous products of photocatalytic oxidation of acrylonitrile on sulfated P25 were CO_2, HCN and HNCO (Jõks et al., 2011). However, there are a few reports of the intermediates of photocatalytic oxidation of acrylonitrile in solution under simulant solar light irradiation.

Fig. 12 illustrates the GC–MS analysis of the decomposition products of acrylonitrile in the presence of N–F codoped TiO_2/SiO_2. Six dominant peaks at 2.55, 2.75, 11.29, 11.68, 12.46 and 14.50 min were detected, and the mass spectral peaks identified the corresponding intermediate compounds as acrylonitrile, acetonitrile, acetic acid, formic acid (or oxalic acid), acroleic acid and acrylamide, respectively. Further confirmation was made by comparing the retention times of pure samples of the intermediates. Most of the intermediates are simple organic acids and less toxic than acrylonitrile. Although several intermediates in the solution were detected, no by-products were detected by GC–MS in the gas phase in the upper reactor during any of the experiments.

The importance of the derivative spectroscopy for interpretation of UV–Vis spectra is well known and documented (Askal et al., 2008). A derivative spectrum can enhance small peaks and shoulders compared to the absorbance spectrum (zero-order band). Derivative spectra can be used to enhance differences among spectra, to resolve overlapping bands in qualitative analysis and, most importantly, to reduce or eliminate background interference from a wide range of sources (Owen, 2000). The most distinctive feature of the second-order derivative is a negative band with minimum at the same wavelength as the maximum on the absorbance band. Perhaps more importantly, derivatives discriminate

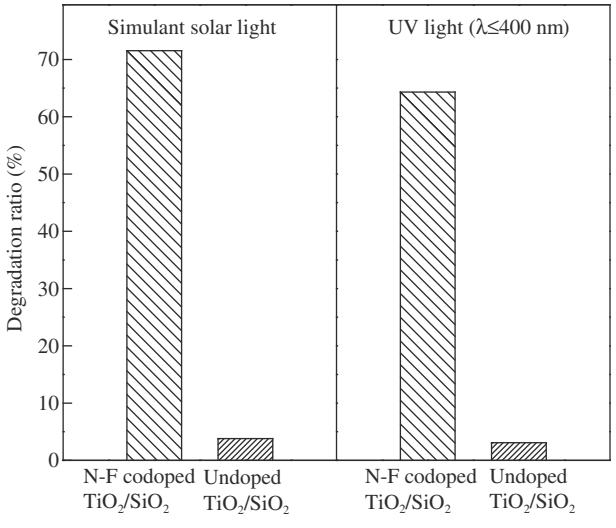

Fig. 11 – Photocatalytic activity of acrylonitrile photodegradation over (a) N–F codoped TiO_2/SiO_2 and (b) undoped TiO_2/SiO_2 samples under simulant solar light and UV light (λ ≤ 400 nm) irradiation, respectively.

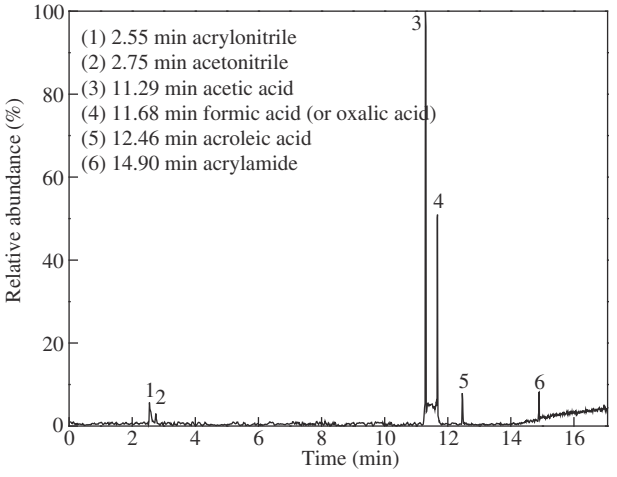

Fig. 12 – GC chromatogram of extract liquid after the photocatalytic decomposition of acrylonitrile with N–F codoped TiO_2/SiO_2.

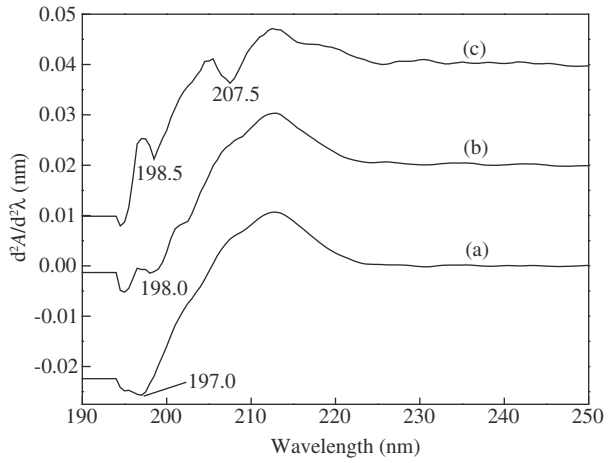

Fig. 13 – Second derivative spectra ($d^2A/d\lambda^2$) of the acrylonitrile solution before adding N–F codoped TiO_2/SiO_2 (a), the solution reaching adsorption equilibrium before irradiation (b) and after exposure to simulant solar light for 6 min (c). *A*: Absorbance; λ: wavelength.

against broad absorbance bands relative to narrow absorbance bands.

The second order derivative spectra of the acrylonitrile solution before adding N–F codoped TiO_2/SiO_2, reaching adsorption equilibrium before irradiation and after exposure to the simulant solar light for 6 min are shown in Fig. 13, respectively. The acrylonitrile solution shows only one peak at 197.0 nm, which is the same as the characteristic absorbance band for acrylonitrile (Fig. 13a). The band for acrylonitrile shifts to longer wavelength after introduction of catalyst and irradiation, which may be due to the presence of the catalyst (Fig. 13b and c). After irradiation, a new strong peak appearing at 207.5 nm is characteristic of the compounds containing an amide group (Owen, 2000). It should belong to acrylamide.

Based on the above results, the study suggests that two distinct pathways might occur during the photocatalytic degradation of acrylonitrile. In the first pathway, some acrylonitrile molecules are converted to acrylamide, when the triple-bonded nitrogen is attacked by ·OH, and then acroleic acid by deamination. Acroleic acid is further oxidized to acetic acid and formic acid (or oxalic acid). In the secondary pathway, some acrylonitrile molecules are oxidized to formic acid and acetonitrile, when the vinyl group is attacked by ·OH. Acetonitrile is further oxidized to acetic acid. The pathways are depicted in Fig. 14.

3. Conclusions

The solid acid catalyst, N–F codoped TiO_2/SiO_2 composite oxide, has been prepared using NH_4F solution as nitrogen and fluorine source. N–F codoped TiO_2/SiO_2 composite oxides show the mesoporous structure. The presence of N–F causes a red shift of the absorption edge for TiO_2/SiO_2 composite oxide. NH_4F concentration and calcination temperature have significant effects on the BET surface area, surface acid sites,

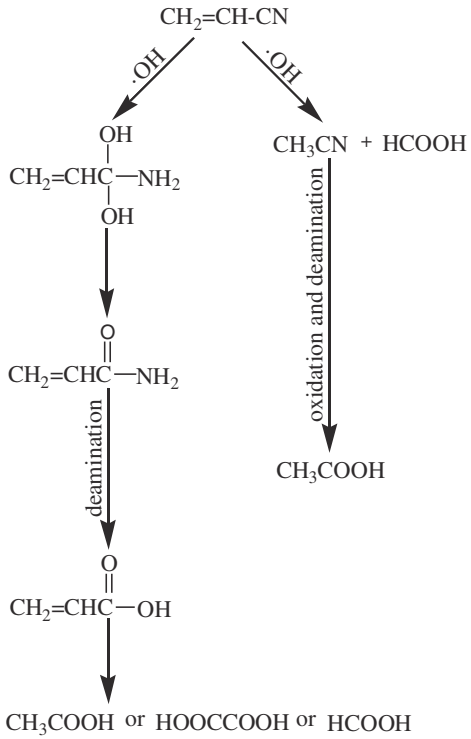

Fig. 14 – Proposed degradation process of acrylonitrile.

crystallinity and the photocatalytic activity of the composite oxides. The *in situ* IR shows that Brønsted and Lewis acid sites appear on the surface of the sample after N–F codoping and they play a crucial role in improving photocatalytic activity. The degradation ratio for acrylonitrile degradation can reach 71.5% after reaction for 6 min under simulant solar light, which indicates that our catalyst is promising for application under solar light. Moreover, the reaction intermediates were verified, and the tentative degradation pathway is proposed for acrylonitrile degradation.

Acknowledgments

This research was financially supported by the Science and Technology Innovation Commission of Shenzhen Municipality, China (No. JCYJ20120613154128107).

REFERENCES

Al-Yassir, N., Le Van Mao, R., Heng, F., 2005. Cerium promoted and silica–alumina supported molybdenum oxide in the zeolite-containing hybrid catalyst for the selective deep catalytic cracking of petroleum naphthas. Catal. Lett. 100 (1-2), 1–6.

Askal, H.F., Refaat, I.H., Darwish, I.A., Marzouq, M.A., 2008. A selective spectrophotometric method for determination of rosoxacin antibiotic using sodium nitroprusside as a chromogenic reagent. Spectrochim. Acta A 69 (4), 1287–1291.

Chen, Y.X., Wang, K., Lou, L.P., 2004. Photodegradation of dye pollutants on silica gel supported TiO_2 particles under visible light irradiation. J. Photochem. Photobiol. A 163 (1-2), 281–287.

Cui, H., Dwight, K., Soled, S., Wold, A., 1995. Surface acidity and photocatalytic activity of Nb_2O_5/TiO_2 photocatalysts. J. Solid State Chem. 115 (1), 187–191.

Gervasini, A., Ragaini, V., 2000. Catalytic technology assisted with ionization/ozonization phase for the abatement of volatile organic compounds. Catal. Today 60 (1-2), 129–138.

Gregg, S.J., Sing, K.W., 1997. Adsorption, Surface Area and Porosity. Academic Press, London, pp. 111–190.

Gu, F., Wang, S.F., Lu, M.K., Zhou, G.J., Xu, D., Yuan, D.R., 2004. Photoluminescence properties of SnO_2 nanoparticles synthesized by sol gel method. J. Phys. Chem. B 108 (24), 8119–8123.

Guo, C.W., Cao, Y., Xie, S.H., Dai, W.L., Fan, K.N., 2003. Fabrication of mesoporous core–shell structured titania microspheres with hollow interiors. Chem. Commun. (6), 700–701.

Huang, C.C., Lin, Y.C., Lu, F.C., 1999. Dynamic adsorption of organic solvent vapors onto a packed bed of activated carbon cloth. Sep. Sci. Technol. 34 (4), 555–570.

Huang, D.G., Liao, S.J., Liu, J.M., Dang, Z., Petrik, L., 2006. Preparation of visible-light responsive N–F-codoped TiO_2 photocatalyst by a sol–gel-solvothermal method. J. Photochem. Photobiol. A 184 (3), 282–288.

Huang, D.G., Liao, S.J., Quan, S.Q., Liu, L., He, Z.J., Wan, J.B., et al., 2007. Preparation of anatase F doped TiO_2 sol and its performance for photodegradation of formaldehyde. J. Mater. Sci. 42 (19), 8193–8202.

Hung, W.C., Chu, H., 2006. Catalytic incineration of acrylonitrile with platinum supported on Al_2O_3. J. Environ. Eng. 132, 1482–1488.

Jang, J.S., Kim, H.G., Ji, S.M., Bae, S.W., Hung, J.H., Shon, B.H., et al., 2006. Formation of crystalline $TiO_{2-x}N_x$ and its photocatalytic activity. J. Solid State Chem. 179 (4), 1067–1075.

Jin, D.F., Gao, J., Hou, Z.Y., Guo, Y., Lu, X.Y., Zhu, Y.H., et al., 2009. Microwave assisted in situ synthesis of USY-encapsulated heteropoly acid (HPW-USY) catalysts. Appl. Catal. A Gen. 352 (1-2), 259–264.

Jõks, S., Krichevskaya, M., Preis, S., 2011. Gas-phase photocatalytic oxidation of acrylonitrile on sulphated TiO_2: continuous flow and transient study. Catal. Lett. 141 (2), 309–315.

Krichevskaya, M., Jõks, S., Kachina, A., Preis, S., 2009. Gas-phase photocatalytic oxidation of acrylonitrile. Photochem. Photobiol. Sci. 8 (5), 600–603.

Le Van Mao, R., Le, T.S., Fairbairn, M., Muntasar, A., Xiao, S., Denes, G., 1999. ZSM-5 zeolite with enhanced acidic properties. Appl. Catal. A Gen. 185 (1), 41–52.

Le Van Mao, R., Al-Yassir, N., Lu, L., Vu, N.T., Fortier, A., 2006. New method for the study of surface acidity of zeolites by NH_3-TPD using a pH-meter equipped with an ion selective electrode. Catal. Lett. 112 (1-2), 13–18.

Léonard, A., Gerber, G.B., Stecca, C., Rueff, J., Borba, H., Farmer, P.B., et al., 1999. Mutagenicity, carcinogenicity, and teratogenicity of acrylonitrile. Mutat. Res. 436 (3), 263–283.

Li, D., Haneda, H., Labhsetwar, N.K., Hishita, S., Ohashi, N., 2005. Visible-light-driven photocatalysis on fluorine-doped TiO_2 powders by the creation of surface oxygen vacancies. Chem. Phys. Lett. 401 (4-6), 579–584.

Li, X.H., Zhang, H.D., Zheng, X.X., Yin, Z.Y., Wei, L., 2011. Visible light responsive N–F-codoped TiO_2 photocatalysts for the degradation of 4-chlorophenol. J. Environ. Sci. 23 (11), 1919–1924.

Macwan, D.P., Dave, P.N., Chaturvedi, S., 2011. A review on nano-TiO_2 sol–gel type syntheses and its applications. J. Mater. Sci. 46 (11), 3669–3686.

Maeda, K., Teramura, K., Takata, T., Hara, M., Saito, N., Toda, K., et al., 2005. Overall water splitting on $(Ga_{1-x}Zn_x)(N_{1-x}O_x)$ solid solution photocatalyst: relationship between physical properties and photocatalytic activity. J. Phys. Chem. B 109 (43), 20504–20510.

O'Regan, B., Grätzel, M., 1991. A low-cost, high-efficiency solar cell based on dye-sensitized colloidal TiO_2 films. Nature 353 (6346), 737–740.

Owen, T., 2000. Fundamentals of Modern UV–Visible Spectroscopy. Agilent Technologies, Germany, pp. 8–12.

Pang, D.D., Wang, Y.T., Ma, X.D., Ouyang, F., 2014. Fluorine promoted and silica supported TiO_2 for photocatalytic decomposition of acrylonitrile under simulant solar light irradiation. Chem. Eng. J. 258, 43–50.

Park, H., Choi, W., 2004. Effects of TiO_2 surface fluorination on photocatalytic reactions and photoelectrochemical behaviors. J. Phys. Chem. B 108 (13), 4086–4093.

Pelaez, M., Nolan, N.T., Pillai, S.C., Seery, M.K., Falaras, P., Kontos, A.G., et al., 2012. A review on the visible light active titanium dioxide photocatalysts for environmental applications. Appl. Catal. B Environ. 125, 331–349.

Saha, N.C., Tomkins, H.C., 1992. Titanium nitride oxidation chemistry: an X-ray photoelectron-spectroscopy study. J. Appl. Phys. 72 (7), 3072–3079.

Tai, Y.W., Chen, J.S., Yang, C.C., Wan, B.Z., 2004. Preparation of nano-gold on $K_2La_2Ti_3O_{10}$ for producing hydrogen from photo-catalytic water splitting. Catal. Today 97 (2-3), 95–101.

Wang, X.C., Yu, J.C., Chen, Y.L., Wu, L., Fu, X.Z., 2006a. ZrO_2-modified mesoporous nanocrystalline $TiO_{2-x}N_x$ as efficient visible light photocatalysts. Environ. Sci. Technol. 40 (7), 2369–2374.

Wang, X.C., Yu, J.C., Liu, P., Wang, X.X., Su, W.Y., Fu, X.Z., 2006b. Probing of photocatalytic surface sites on SO_4^{2-}/TiO_2 solid acids by in situ FT-IR spectroscopy and pyridine adsorption. J. Photochem. Photobiol. A 179 (3), 339–347.

Wu, Y.M., Xing, M.Y., Tian, B.Z., Zhang, J.L., Chen, F., 2010. Preparation of nitrogen and fluorine co-doped mesoporous TiO_2 microsphere and photodegradation of acid orange 7 under visible light. Chem. Eng. J. 162 (2), 710–717.

Xiang, Q.J., Lü, K.L., Yu, J.G., 2010. Pivotal role of fluorine in enhanced photocatalytic activity of anatase TiO_2 nanosheets with dominant (001) facets for the photocatalytic degradation of acetone in air. Appl. Catal. B 96 (3-4), 557–564.

Xie, Y., Li, Y.Z., Zhao, X.J., 2007. Low-temperature preparation and visible-light-induced catalytic activity of anatase F–N-codoped TiO_2. J. Mol. Catal. A 277 (1-2), 119–126.

Yu, J.C., Yu, J.G., Ho, W.K., Jiang, Z.T., Zhang, L.Z., 2002. Effects of F doping on the photocatalytic activity and microstructures of nanocrystalline TiO_2 powders. Chem. Mater. 14 (9), 3808–3816.

Zhang, J., Pierce, G.E., 2009. Laboratory-scale biofiltration of acrylonitrile by *Rhodococcus rhodochrous* DAP 96622 in a trickling bed bioreactor. J. Ind. Microbiol. Biotechnol. 36 (7), 971–979.

Zhang, W.F., Zhang, M.S., Yin, Z., Chen, Q., 2000. Photoluminescence in anatase titanium dioxide nanocrystals. Appl. Phys. B 70 (2), 261–265.